







Article

Au/Ti Synergistically Modified Supports Based on SiO₂ with Different Pore Geometries and Architectures

Gabriela Petcu¹, Elena Maria Anghel¹ , Elena Buixaderas² , Irina Atkinson¹ , Simona Somacescu¹, Adriana Baran¹, Daniela Cristina Culita¹ , Bogdan Trica³ , Corina Bradu⁴, Madalina Ciobanu¹  and Viorica Parvulescu^{1,*}

¹ Institute of Physical Chemistry “Ilie Murgulescu” of the Romanian Academy, 202 Splaiul Independentei st., 060021 Bucharest, Romania

² Institute of Physics, Czech Academy of Sciences, Na Slovance 2, 18200 Prague, Czech Republic

³ National Institute for Research & Development in Chemistry and Petrochemistry-ICECHIM, Spl. Independentei 202, 060021 Bucharest, Romania

⁴ Research Center for Environmental Protection and Waste Management, University of Bucharest, Spl. Independentei 91-95, 050095 Bucharest, Romania

* Correspondence: vpirvulescu@icf.ro

Abstract: New photocatalysts were obtained by immobilization of titanium and gold species on zeolite Y, hierarchical zeolite Y, MCM-48 and KIT-6 supports with microporous, hierarchical and mesoporous cubic structure. The obtained samples were characterized by X-ray diffraction (XRD), N₂-physisorption, scanning and transmission electron microscopy (SEM/TEM), diffuse reflectance UV-Vis spectroscopy (DRUV-Vis), X-ray photoelectron spectroscopy (XPS), Raman and photoluminescence spectroscopy. The photocatalytic properties were evaluated in degradation of amoxicillin (AMX) from water, under UV (254 nm) and visible light (532 nm) irradiation. The higher degradation efficiency and best apparent rate constant were obtained under UV irradiation for Au-TiO₂-KIT-6, while in the visible condition for the Au-TiO₂-MCM-48 sample containing anatase, rutile and the greatest percent of Au metallic clusters were found (evidenced by XPS). Although significant values of amoxicillin degradation were obtained, total mineralization was not achieved. These results were explained by different reaction mechanisms, in which Au species act as e⁻ trap in UV and e⁻ generator in visible light.

Keywords: zeolite Y; hierarchical zeolite Y; 3D mesoporous silica; Au/Ti-supported catalysts; surface plasmon resonance effect; photocatalytic degradation of amoxicillin



Citation: Petcu, G.; Anghel, E.M.; Buixaderas, E.; Atkinson, I.; Somacescu, S.; Baran, A.; Culita, D.C.; Trica, B.; Bradu, C.; Ciobanu, M.; et al. Au/Ti Synergistically Modified Supports Based on SiO₂ with Different Pore Geometries and Architectures. *Catalysts* **2022**, *12*, 1129. <https://doi.org/10.3390/catal12101129>

Academic Editor: Valentin Valtchev

Received: 31 August 2022

Accepted: 21 September 2022

Published: 28 September 2022

Publisher's Note: MDPI stays neutral with regard to jurisdictional claims in published maps and institutional affiliations.



Copyright: © 2022 by the authors. Licensee MDPI, Basel, Switzerland. This article is an open access article distributed under the terms and conditions of the Creative Commons Attribution (CC BY) license (<https://creativecommons.org/licenses/by/4.0/>).

1. Introduction

Active photocatalysts were obtained by supporting gold species, either on active (TiO₂) [1,2] or inert (SiO₂) [3] oxides. Activity of the Au-TiO₂ photocatalysts is a function of different parameters, such as electronic factors, gold and titania dispersion and interaction [4]. An important strategy to ensure highly dispersed gold species is selection of a suitable support with high surface area, enabling control of the supported particle size and agglomeration rate. Furthermore, it was reported [5] that TiO₂ presence on different supports is beneficial not only for photocatalytic activity but also in catalyst manufacturing by improving dispersion of the gold species. It was noticed that TiO₂ particles play a dual role in gold immobilization on silica support. Thus, TiO₂ particles, evenly dispersed into silica mesopores, act as a scaffold [6], preventing silica framework to collapse and there are an anchor able to interact with Au species. High dispersion of TiO₂ is a key factor because gold nanoparticles (AuNPs) interact preferentially with Ti sites. Thus, Au/Ti synergistically modified supports based on SiO₂, with different pore geometries and architectures, can enhance the photocatalytic performances under visible light conditions and represent a promising solution in environmental remediation area. The support porosity affects the

size of immobilized TiO₂ particles due to the confinement effect inside the pores and accessibility of gold species to TiO₂ sites, leading to different interaction between titanium and gold as a function of the support nature. Great attention was paid to mesoporous silica due to its specific properties as high surface area and porosity, ordered porous structure and controllable pore size [7,8]. The previous studies [9–11] show that TiO₂ loading within SiO₂ support ensures modification of the charge carrier dynamics by reductions in recombination intensity and increases in charge carrier lifetime due to the impact with the support electric field. Thus, mesoporous silica is considered an ideal support for a high dispersion of metal on its surface, leading to achievement of catalytic materials with high performances [12]. Among the various ordered mesoporous silica, MCM-48 and KIT-6 materials are more suitable for photocatalytic applications due to their cubic arrangement and highly connected open porous networks, which provide a better access of light irradiation and reactants to the active sites [9,13]. In addition to that, the mesoporous silica with cubic structure favors the formation of a high amount of titania species with tetrahedral coordination, considered to be more photocatalytically active than octahedral coordinated TiO₂ [14]. In comparison with mesoporous silica support, a more homogeneous dispersion of TiO₂ was achieved using zeolites with microporous structure and high crystallinity degree [15]. However, in catalytic applications, zeolites have the disadvantage of limiting the pore access for reactants with larger molecules. In order to overcome this drawback, hierarchical zeolites were developed [16,17]. These materials preserve the advantages of zeolites as well as mesoporous silica materials, favoring the mass transfer of reactants. Further, mesoporous systems allow for an efficient adsorption/desorption process of the reactants/products [17]. The adsorption of reactants on a photocatalyst is a key step because photogenerated charge carriers have a short lifetime, so only those molecules adsorbed on the surface of the photocatalyst near the active sites can take part in the photocatalytic process.

The Au-TiO₂ system was intensively studied and used in wide applications as photocatalytic degradation of different pollutants (azo dyes, chloroaromatic compounds, phenol) from wastewater under visible or UV irradiation [18–20], hydrogen production [18] or photocatalytic reduction of CO₂ [12]. Associated with titanium, gold was supported on mesoporous silica materials as SBA-15 [21,22], MCM-41 [23] and microporous TS-1 zeolite [24]. However, from our knowledge, any comparative study has not been reported yet on the effects of support properties on Au-TiO₂ photocatalytic activity. No catalytic systems were obtained by immobilizing Au-TiO₂ on supports, such as zeolite Y, hierarchical zeolite Y and ordered cubic mesoporous silica (KIT-6 and MCM-48) supports. Therefore, in this work, new photocatalysts were obtained by immobilization of titanium and gold on the supports with various porous structure (micropores—zeolite Y, micro and mesopores—hierarchical zeolite Y, smaller mesopores—MCM-48 and larger mesopores—KIT-6). Zeolite Y exhibits a faujasite (FAU) framework with three-dimensional porous structure [25]. For comparison, two types of mesoporous silica support (MCM-48 and KIT-6), with 3D structure and smaller, respectively, larger mesopores, were selected. In addition to the porous structure, the surface properties were also varied by a change of the surfactant and by incorporation of aluminum in the silica network during the zeolite synthesis. The effects of porous structure and surface properties on TiO₂ dispersion, crystal structure, nature of interaction between support–titanium species and Au-TiO₂, respectively, were studied. Further, we investigated the influence of support properties, the presence of TiO₂ and Au species and their interaction on amoxicillin (AMX) photodegradation under UV and visible light irradiation as a model reaction for applications of these materials in degradation of organic compounds from contaminated water. Amoxicillin is a β -lactam antibiotic from the penicillin class with a broad spectrum and applications in veterinary and human medicine, hardly degradable and its removal from wastewater represents a real interest [26]. The effect of porous structures and adsorption on performances in photocatalytic degradation of amoxicillin (AMX) was also evidenced in previous studies [16,26] and formed the basis of the applications herein studied.

2. Results and Discussion

2.1. Properties of Supported Au/Ti Photocatalysts

X-ray patterns at wide angle of all samples, except that supported on KIT-6, present three distinct diffraction lines at $2\theta \approx 25.2, 37.8, 48.1^\circ$, indexed to (101), (004) and (200) crystal planes of anatase TiO_2 phase (Figure 1A). No reflections ascribed to TiO_2 were detected in the XRD pattern of the KTA sample. This may be the result of the high dispersion of titanium on KIT-6 mesoporous support surface with higher concentration of the silanol group. It has been shown that the ability of silica surface for chemical modification is determined by the content of silanol groups Si–OH [27]. The comparative study of two silicas (MCM-41, SBA-15) with hexagonal ordered mesoporous structure explained the decreasing of silanol density for MCM-41 by zeolitization of this silicate obtained in basic conditions. Moreover, the concentration of surface hydroxyl groups increased for MCM-48 compared to MCM-41 due to the disorder in its porous structure [28]. Therefore, we can consider that, among the mesoporous supports used, KIT-6 has a higher concentration of silanol on the surface, as it was demonstrated further by Raman spectroscopy (Figure S6a).

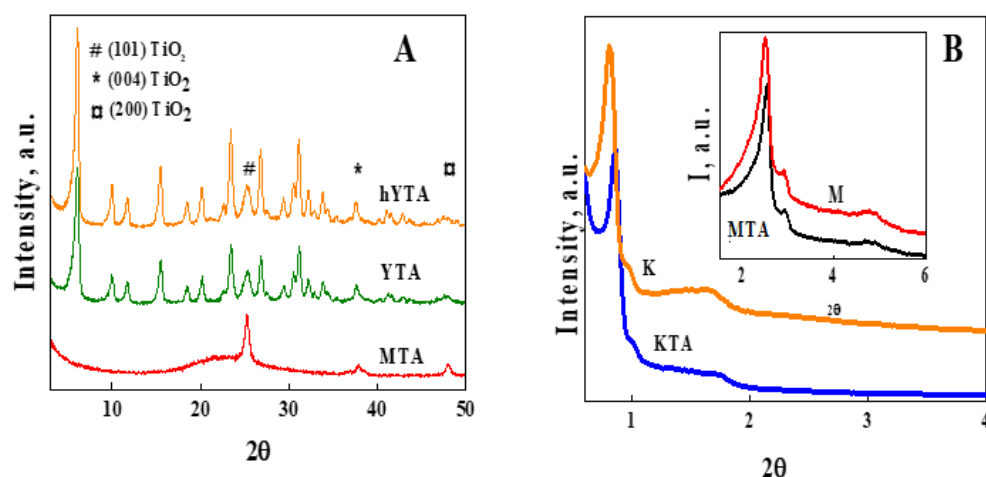


Figure 1. XRD patterns at wide angle (A) and low angle (B) of synthesized materials.

One can notice that gold-based compounds were not identified in the XRD patterns. The absence of gold reflections can be a consequence of the high dispersion of gold nanoparticles and their low content (<1%), below the limit of detection for XRD analysis [29]. The presence of Ti and Au in all the samples was confirmed by TEM-EDX data (Figure S1).

The XRD patterns of the synthesized photocatalysts showed that structure of the porous supports was insensitive to incorporation of the Ti and Au species. Wide-angle XRD patterns (Figure 1A) of photocatalysts supported on zeolite Y (YTA) and hierarchical zeolite Y (hYTA) have similar diffraction patterns with the corresponding supports [15]. Further, low-angle XRD patterns (Figure 1B) highlight the preservation of MCM-48 and KIT-6 ordered cubic mesoporous structure [7,13] for MTA and KTA samples.

TEM images of the porous host structure after immobilization of Ti and Au species are illustrated in Figure 2. Figure 2A shows the mesoporous cubic-ordered structure of KIT-6 and Figure 2B shows the crystalline structure of zeolite Y. The mesoporous structure of MCM-48 and hierarchical zeolite Y supports, respectively, the crystals from the last one, are illustrated in Figure S2.

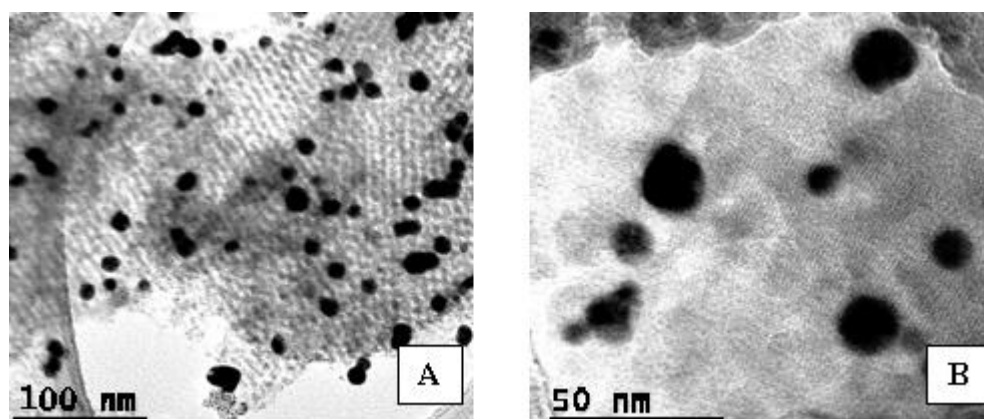


Figure 2. TEM images of KTA (A) and YTA (B) samples.

According to IUPAC classification, N_2 adsorption–desorption isotherms of Ti–Au photocatalysts (Figure 3) exhibit type IV isotherm with H1 hysteresis loop for materials based on KIT-6 and H3 for the ones based on MCM-48. Analogous N_2 adsorption–desorption isotherms with hysteresis loops of both supported catalysts and their corresponding mesoporous supports imply that shape and pore dimension were not altered by titanium and gold immobilization.

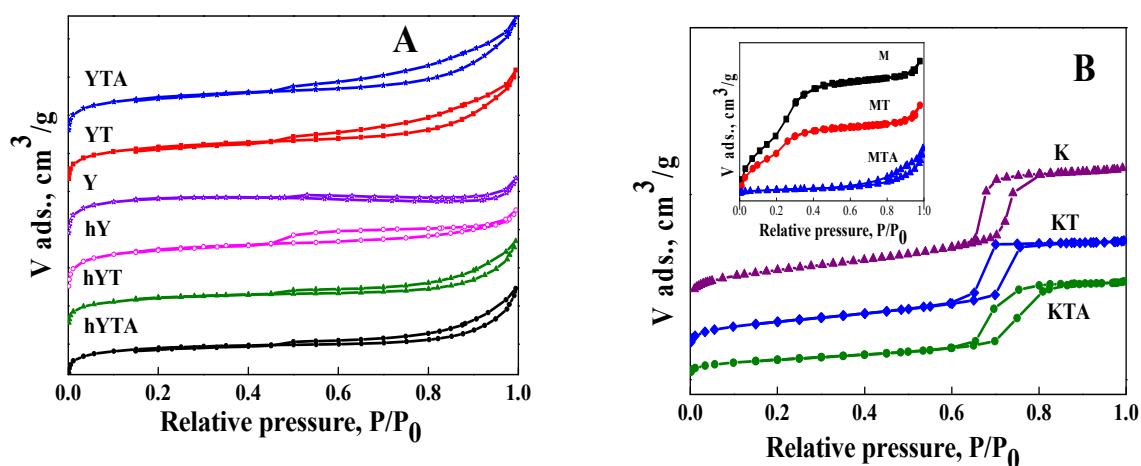


Figure 3. N_2 adsorption–desorption isotherms of the photocatalysts with zeolite Y supports (A) and mesoporous silica supports (B) MCM-48 (M) and KIT-6 (K).

Conversely, a hysteresis loop came out after TiO_2 immobilization on zeolite Y (Figure 3A), very likely due to mesopores formed among TiO_2 nanoparticles. After gold immobilization on MT, the N_2 adsorption–desorption isotherm does not maintain the step inflection at the relative pressure near P/P_0 0.25–0.3 as a support isotherm (inserted isotherms in Figure 3B), indicating that metallic species are not immobilized in the pores as an ideally homogeneous layer [30], but rather form deposits at their entrance and out of them. However, titania and gold immobilization caused a more significant decrease in pore volume (Figure 3B) of the MCM-48 support (MT and MTA samples), as opposed to the other mesoporous supports used, e.g., KIT-6. This is due to smaller pore size of MCM-48 compared to KIT-6, as depictable in Table S1, for 10% titania loading. Our previous study on MCM-48-supported catalysts [13] pointed out a smaller decrease in pore volume in conditions of a lower TiO_2 loading (5%). The zeolite-supported catalysts show a combination of type I and IV isotherms with H3 and H4 hysteresis loop [14]. The absence of the adsorption hysteresis for MCM-48 and Ti-MCM-48 samples is a result of their uniform pore distribution. Values of surface areas and pore size after each impregnation step are summarized in Table S1. Further immobilization of gold caused a BET surface increase for the zeolite-

supported samples in contrast with the mesoporous ones. The latter finding confirms gold immobilization on titania.

Morphology of the synthesized samples after titanium and gold immobilization is presented in Figure 4. No change in morphology was observed after the impregnations of supports. Thus, the preservation of octahedral morphology with smooth surface, specific to zeolite Y and no aggregates or any other observable defects in the structure of zeolite Y was evidenced. Further, SEM images of KTA and MTA samples revealed typical morphology of MCM-48 and KIT-6 mesoporous silica, respectively [13,31].

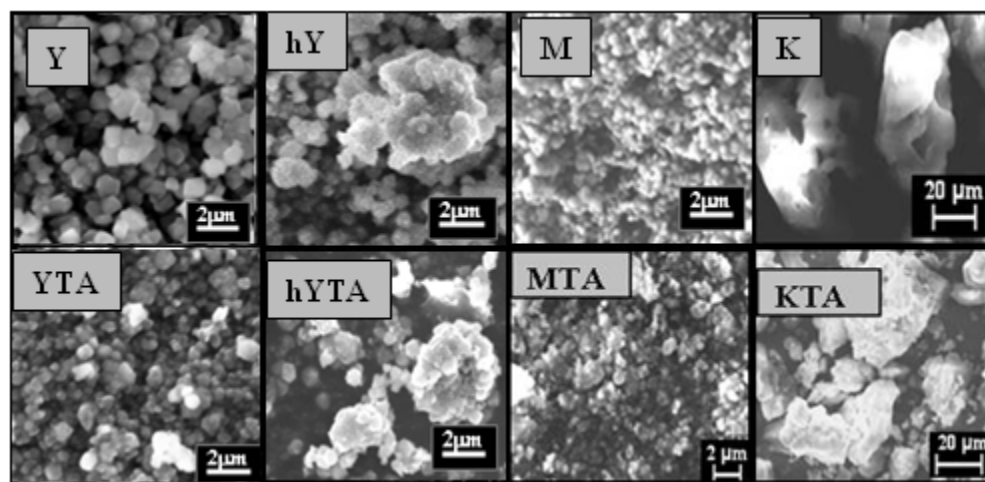


Figure 4. SEM images of the synthesized photocatalysts.

TEM images show a high dispersion of gold nanoparticles with diameters ranging from 5 to 24 nm for samples supported on KIT-6 and zeolite Y (Figure 2). Larger Au particles and association of Au-NPs (clusters) on hYT and MT supports are more obvious (Figure S2). These facts are in agreement with the XPS results from Table 1.

Table 1. XPS data: binding energies (BEs) and the quantitative assessment.

Sample	Binding Energy (eV)				Au Chemical Species rel.conc.			
	Au4f/2 Metallic nps	Au4f/2 Clusters	Au4f/2 Au ⁺	Au4f/2 Au ³⁺	Au Metallic nps	Clusters	Au ¹⁺	Au ³⁺
YTA	83.3	84.3	85.3	86.7	44.7	18.8	18	18.6
hYTA	83.3	84.3	85.3	86.7	-	60.2	-	39.8
MTA	83.3	84.3	85.3	86.7	-	63.9	-	36.1
KTA	83.3	84.3	85.3	86.7	64.8	-	-	35.2

A higher content of Au clusters on the surface of the hYTA and MTA samples was depicted. XPS spectroscopy provides evidence for the low relative concentrations (<1%) of gold on the sample surface (<10 nm) as the photoelectron spectra are very noisy despite the large number of runs recorded during data acquisition. Moreover, the “band-like” shape of the Au4f spectra suggests the presence of different chemical species accommodated under the experimental spectra envelope.

XPS spectra for the synthesized samples presented in Figure S3 show four types of chemical species, as follows: Au metallic nanoparticles (4 nm), very small Au^{δ+} clusters as well as Au¹⁺ and Au³⁺ oxidation states [32,33].

One can notice that a higher Au content favors the formation of additional species, such as: cluster type Au, Au¹⁺ and Au³⁺ oxidation states. As XPS data showed (Table 1), different gold species were obtained as a result of their interaction with TiO₂ supported on different porous materials. In heterogeneous catalytic processes, a key factor that

deserves great attention is the interaction between metallic species and oxide supports, the phenomenon known as strong metal–support interaction (SMSI), which implies an electron transfer between support and metal species immobilized. The SMSI phenomenon has an important role in photocatalyst stability and activity [34].

A close examination of the Au 4f spectral deconvolution suggests the influence of the synthesis procedure on the Au surface chemical species. In addition to the synthesis conditions, the nature of the surfactant leads to specific properties of the support (pore size and shape, volume and specific area, morphology, stability and surface properties) that influence the dispersion and nature of the titanium species and finally the gold ones. The dispersed titanium species represent a support for gold, their interaction being a strong one (SMSI). Thus, the samples hYTA and MTA whose supports were obtained using a cationic surfactant (TTAB and CTAB, respectively) display similar chemical species. Unlike these, the KTA sample (with support KIT-6 obtained using P123 nonionic surfactant) possesses the highest amount of metallic gold on the surface.

The surface chemistry of titanium, oxygen and silicon is assessed in Figure S4a–c. The two Ti2p peaks indicated that 4+ is the only oxidation state of titanium (Figure S4a). Ti⁴⁺ from Ti–O–Ti oligomers is represented in octahedral coordination (lower binding energy), while Ti⁴⁺ from the isolated Ti–O–Si sites is in tetrahedral (higher binding energy) coordination [35,36]. The ratio of these peak intensities indicates a small variation with titania loading. The lower concentration of TiO₂ on the surface of the KTA sample, accessible to XPS measurements, represents another argument regarding its homogeneous distribution on the silica surface as Ti–O–Si species. Although the Ti content is similar to that of the zeolite samples (YTA, hYTA), the highest percentage of TiO₂ on the surface was evidenced for the MTA sample (Figure S4b). This confirms a different interaction of titanium with the surface of the support. In the case of the latter support, the agglomerated oxide species predominate on the surface. Figure S5a–d show the deconvoluted O1s spectrum for all the samples under investigation. For KTA and MTA samples, a peak at ~533 eV is attributed to the O–Si bond from siliceous mesoporous supports (MCM-48, KIT-6), while the peak at a lower BE (~532.5 eV) is assigned to O–Si from zeolite supports. The oxygen peak located at ~530 eV indicates the presence of oxygen bonded to Ti in TiO₂ species with octahedral coordination. The OH groups adsorbed on the TiO₂/SiO₂ surface were detected at ~531.2 eV and in a range 533–534 eV, respectively. We emphasize that in the range 533–534 eV, traces of water adsorbed from the environment might be present on the porous silica surfaces. In order to distinguish between OH bonded as silanol in the sample lattice and the OH from adsorbed water, Raman spectroscopy was used (Figure S6c). For the KTA sample, the presence of both OH group types was evidenced; however, the narrow peak located at 3741 cm⁻¹ suggests a higher content of OH from mesoporous silica lattice compared to zeolite Y, for which more adsorbed water is observed, or the YTA sample, which does not present silanol groups. Two distinct binding energies (BEs) were evidenced for Si2p XPS spectra (Figure S4b). The peak from higher BEs (103.2 eV) was assigned to Si–O from MCM-48 and KIT-6 mesoporous silica supports and the one from lower BEs (102.3 eV) to Si–O from zeolite supports. In the case of zeolite samples, the shift in peaks recorded by O1s and Si2p high-resolution XPS spectra is the result of Al³⁺ effect, which reduces the energy in the O–Si bond. Figure S4c shows the presence of aluminum (in a smaller amount than silicon) on the surface of the samples obtained using Y-type zeolite as a support.

Visible Raman spectra of the (Y/hY/K/M)TA powders are illustrated in Figure 5. The ultralow frequency peaks within 12–16 cm⁻¹ (inset of the Figure 5) are due to surface vibrations in the particle pore structures [37–39]. Further, a densification process and, hence, enhancement in the nanoparticle sizes give rise to a lower-wavenumber shift in this peak. Consequently, the cubic KTA is expected to have smaller nanoparticle sizes of TiO₂ and/or bigger pore size than the other cubic sample, MTA. This is analogous to the low-angle XRD findings in Figure 1B where the lowest shifted peak (below 1°) due to d₂₁₁ plane signifies bigger pore size in the KTA sample in contrast with MTA (peak located above 2°).

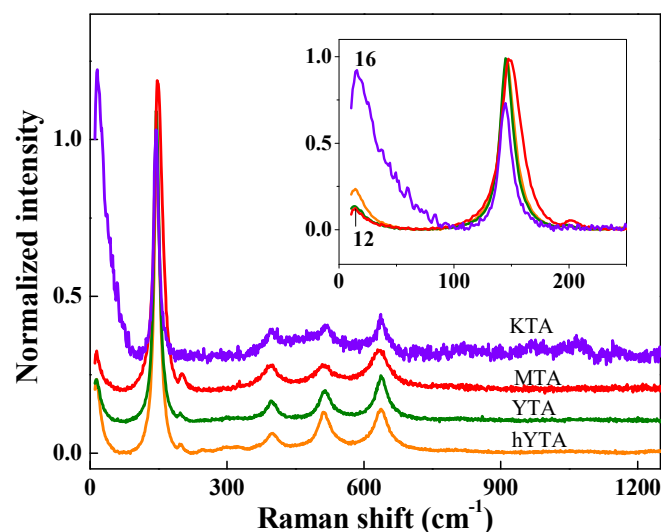


Figure 5. Raman spectra of the (K/M/Y/hY)TA catalysts (laser line of 514 nm).

The non-framework anatase modes (E_g located at 144, 197 and 640 cm^{-1} , B_{1g} at 400 and 519 cm^{-1} and A_{1g} at 507 cm^{-1} [40]) were identified in the Raman spectra of the (K/M/Y/hY)TA samples. Since the 197 cm^{-1} peak is not visible for the KTA sample, there is a phonon confinement effect typically present in the case of TiO_2 [41], for a grain size of only a few nanometers. Despite the strong Raman scattering of anatase, small spectral features of silica support are noticeable in the Raman spectrum of KTA_514 (Figures 5 and S6a) above 750 cm^{-1} . This is a consequence of the most pronounced plasmon resonant effect induced by gold [42] into the KTA catalyst, i.e., the 514 nm laser line used to excite sample is close to the $\sim 550\text{ nm}$ absorption in Figure 6, as well as modification of the internal porosity of silica support by titania. The 144 , 400 and 640 cm^{-1} modes of anatase are very sensitive to the crystallite size [43]. A wider peak at about 150 cm^{-1} in the case of the MTA might point out anatase nanoparticles smaller than 10 nm . Further, the presence of rutile in the MTA catalyst is confirmed by its shifted 633 cm^{-1} band [43] in Figure 5 and 616 cm^{-1} band in the UV-Raman spectrum in Figure S6. An enhanced 513 cm^{-1} band for hYTA shows the presence of oxygen motion in a plane bisecting T–O–T bonds (T represents Si and/or Al) [44] in zeolites. A tiny peak at 324 cm^{-1} could be attributable to ring breathing via Si–O–Si linkages [44] in zeolites.

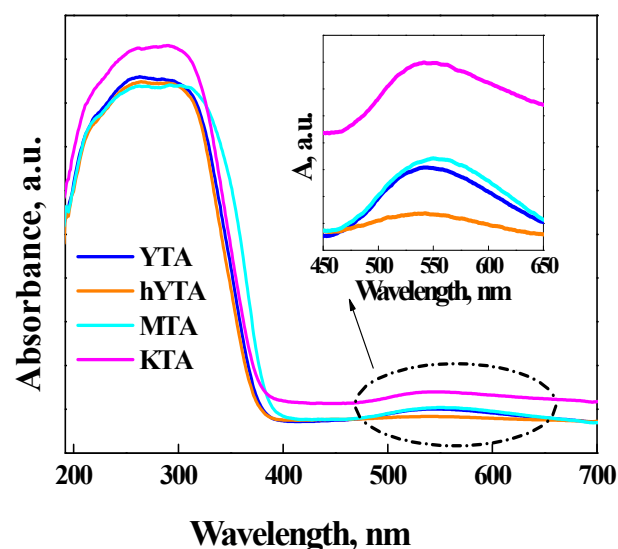


Figure 6. UV-Vis spectra of Ti-Au photocatalysts.

UV-Raman bands of the KA sample, obtained by immobilization of gold on KIT-6 support, are located at 385, 447, 492 and 603 cm^{-1} in Figure S6a, being assignable to six-, five-, four- and three-membered siloxane rings [45,46]. The latter bands are also named defect bands, D₁ and D₂ [46]. The next bands at 791 and 823 cm^{-1} belong to Si-O-Si linkages, while the 973 cm^{-1} band originates from stretching modes on the surface silanols, O₃Si-OH [45,47]. Thus, in comparison with the MTA sample, a higher silanol group content on KTA can be observed. The presence of the silanols is also supported by the high wavenumber band at 3741 cm^{-1} (Figure S6c), assignable to stretching of SiO-H linkages. Typically, UV-Raman investigations are used to remove a fluorescent background and identify possible highly dispersed titanium oxide and/or titanium ions in the micro- and mesoporous frameworks of supports [48]. Thus, loading of TiO₂ into mesoporous silica support should cause a diminishing of the 980 cm^{-1} band and/or shifting towards lower wavenumbers [47] due to gradual interaction with a Ti cation (Si-O^{δ-} ... Ti^{δ+}) [49]. Since the intensity of the 971 cm^{-1} seems less affected in the case of the KTA spectrum, Ti atoms are very likely incorporated in the KIT-6 framework rather than interacting with surface silanol. No band at about 980 cm^{-1} but a wide band peaking up at 921 cm^{-1} is depicted for MTA in Figure S6a. Bands at 490, 542 and 1124 cm^{-1} are considered to belong to Si-O-Ti linkages [48,49]. It is obvious that UV-Raman is sensitive to the KIT-6 and MCM-48 supports of the KTA and MTA catalysts. Conversely, TiO₂ loading of the zeolite supports caused surface silanol interaction (see Figure S6b) meaning that the 970 cm^{-1} band vanishes. Non-framework anatase is noticeable in both visible and ultraviolet Raman spectra of the (M/K/Y/hY)TA catalysts.

UV-Vis diffuse reflectance spectra of the photocatalysts obtained by immobilization of Au-TiO₂ active species on micro/meso/micro and mesoporous supports are presented in Figure 6.

For all photocatalysts, a high absorption capacity was recorded in the UV domain, revealing a broad absorption band, resulting from overlapping of more absorption bands related to several titanium species. Three main absorption peaks can be observed for the synthesized samples around 220, 260 and 310 nm. The UV signal at around 220 nm was associated to tetrahedral Ti species, while the absorption peak at around 260 nm was related to octahedral Ti-oxide species. The shoulder of absorption presented after 300 nm indicates the presence of a TiO₂ anatase phase on the support surface [14,21]. Furthermore, for the MTA sample, a red shift in the absorption bands was shown, corresponding to an increase in TiO₂ particle size, as evidenced using the Scherrer equation (Table S1). This behavior was explained by the quantum size effect that emerges for TiO₂ species with particle sizes <10 nm [15]. After Au immobilization, a specific band absorption in the visible domain, at around 550 nm, was observed. This weak signal recorded in the visible region is due to the surface plasmon resonance effect of gold nanoparticles [12]. This effect is determined by gold particles composition and size and their interaction with titania from the support [21]. These results are in agreement with those obtained by XPS spectroscopy (Table 1).

A better interaction between gold nanoparticles and material used as support leads to a higher stabilization with an increase in corresponding signal intensity [12]. The highest peak assigned to the plasmonic effect of gold nanoparticles was obtained for the photocatalyst supported on KIT-6. XPS results (Table 1) show the highest Au-NPs concentration on the surface for this sample. Gold nanoparticles have a better interaction with titanium species, being highly dispersed, as XRD results revealed. The intensity of the Au plasmonic effect decreased as follows: KTA > YTA ≥ MTA > hYTA. This variation can be very well correlated with the nature of the titanium (Figure S4a) and gold (Table 1) species on the surface. The highest intensity of the plasmonic effect for the KTA sample is due to a high dispersion of titania and, consequently, to the presence of the highest percent of Au metallic nanoparticles.

The band gap energy of photocatalysts was obtained using the Kubelka-Munk function by plotting $[F(R) \cdot hv]^{1/2}$ versus photon energy (eV). As shown in Table 2, a narrowing of the band gap was obtained after titanium immobilization on porous supports in com-

parison with bulk TiO_2 (3.2 eV) due to the high dispersion of titania as tetrahedral Ti-O-Si species [36,50]. The values of band gap energy depend on the physico-chemical properties of porous supports. Further, after gold immobilization, a widening of the band gap values for the all photocatalysis was evidenced. This behavior can be explained by the Burstein–Moss (BM) effect [51], as a result of plasmonic properties of gold nanoparticles.

Table 2. Band gap energy of photocatalysts.

Sample	YT	hYT	KT	MT
Eg (eV)	3.17	3.22	3.14	3.13
Sample	YTA	hYTA	KTA	MTA
Eg (eV)	3.20	3.26	3.19	3.17

Practically, under light irradiation, the conduction band of TiO_2 is filled by free electrons of Au nanoparticles. Therefore, since the conduction band of TiO_2 is blocked, the transitions of electrons from the valence band are allowed only at energy levels higher than the Fermi level. Therefore, the energy required for electron transitions must be large enough to allow the electron transfer to occur not just up to the conduction band, but up to a higher free energy level.

Photoluminescence (PL) spectra were measured to show the effect of active species and support on light-generated electrons and holes, since PL emission is a result of the recombination of the free carriers. The key factors for conjunction of the photoluminescence effect are considered the oxygen vacancies concentration [52,53]. These defects are trapping centers, which inhibit the recombination and simultaneously enable efficient joining electrons with the oxygen, which is why they are considered as active centers for the adsorption on the surface of water and OH^- groups necessary for carrying out the photocatalytic reaction.

The photoluminescence results recorded after TiO_2 immobilization on different supports (Figure 7A) show the lowest emission for the MT sample with TiO_2 as a mixture of anatase and rutile crystalline species. This indicates that by supporting TiO_2 on MCM-48 mesoporous silica, the recombination of photogenerated charges was suppressed.

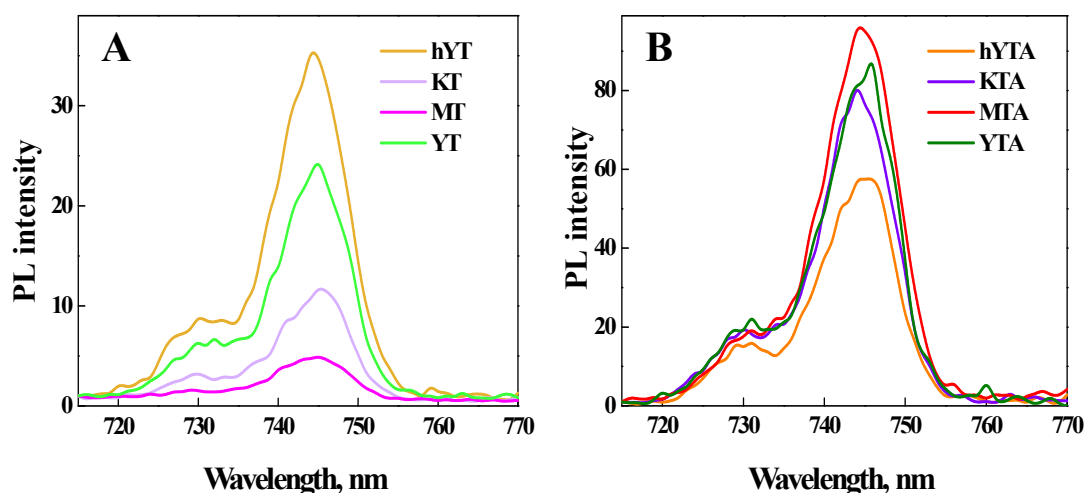


Figure 7. The PL spectra of Ti-modified materials (A) and Au-Ti photocatalysts (B).

For all gold-modified photocatalysts, the enhancement in PL emission was observed (Figure 7B), which can be explained by changes in the level of surface defects, due to the interaction between Au nanoparticles— TiO_2 with higher particle size and different numbers and types of surface defects. The reduction in surface defects enhances the electron number, available to recombine with the holes, leading to an enhancement in the

near-band-edge emission [54]. A different number of oxygen vacancies could be created by TiO_2 immobilization, as a result of different interaction between TiO_2 and silica supports. The electron pair remained in the vacancy after oxygen defect formation at the interface of $\text{TiO}_2/\text{SiO}_2$ moves toward the neighboring Ti atoms, creating reduced Ti^{3+} and Ti^{2+} species.

2.2. Adsorption and Photocatalytic Activity

The AMX adsorption on the obtained materials was evaluated in dark conditions. The obtained results on the adsorption increasing in time are presented in Figure 8.

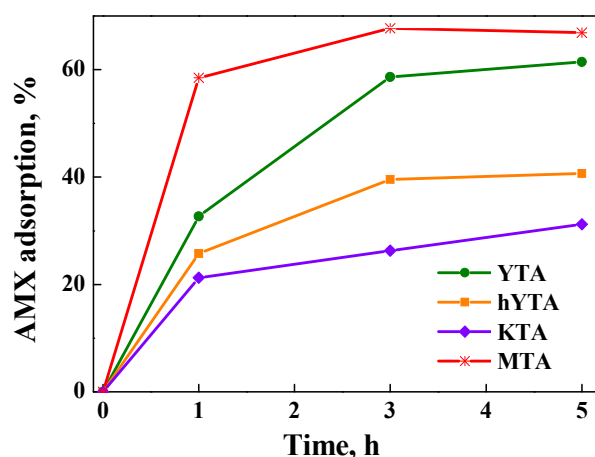


Figure 8. Adsorption capacity of photocatalysts in amoxicillin degradation.

There is a significant increase in adsorption during the first hour, after which the variation is insignificant, tending to a level reached after three hours for all samples. The adsorption capacity increased in the following order: $\text{KTA} < \text{hYTA} < \text{YTA} < \text{MTA}$.

The higher degradation rate of antibiotics obtained for supported TiO_2 on zeolites and mesoporous silica was attributed to the higher adsorption capacity of the supports [55,56]. The dominant adsorption mechanism was attributed to the electrostatic interaction and H-bonding between ionized and unionized molecules of AMX and active groups from the support surface in acidic ($\equiv\text{Si-OH}^{2+}$) or basic conditions ($\equiv\text{Si-O}^-$) [57]. Additionally, the Brønsted acid sites due to the $\equiv\text{Si-OH-Al}\equiv$ group in the zeolite framework can be easily deprotonated to form $\equiv\text{Si-O}^-$ [58]. In AMX solution ($\text{pH} = 7.2$), the surface of supports is negatively charged and adsorption is the result of interaction between this deprotonated oxygen and hydrogen atoms from AMX antibiotic, weakly bound to O or N, as a result of intramolecular electronic effects (Figure S7). Therefore, when the photocatalyst is added to the AMX solution, the pH is increased to 9.4. Over time, there is a slight decrease in pH in both cases of adsorption and photocatalytic reaction. It was observed that after 5 h, the pH value was around 8.

Therefore, TiO_2 supporting on different materials determines both the number of centers and their strength. A different number of oxygen vacancies could be created by immobilization of TiO_2 on zeolite Y, as a result of interaction between TiO_2 and support. The electron pair remained in the vacancy after oxygen defect formation at the interface of TiO_2 and SiO_2 moves toward the neighboring Ti atoms [59].

In degradation of organic compounds from wastewater, adsorption and photocatalytic processes act simultaneously and the results showed a synergistic effect of these [60]. The processes that take place in degradation of amoxicillin (AMX) from water are presented in Figure S8 for the YTA sample. It can be seen that in the first 3 h, the variation in AMX concentration is strongly determined by adsorption. After 3 h, the significant decrease in concentration can be considered only as a result of the photocatalytic process. In photocatalytic degradation of AMX, adsorption can be considered as a rate-determining step. It has been shown that, depending on the photocatalytic process, its relationship with adsorption can be proportional or contradictory [61]. Because amoxicillin adsorption could

be the rate-determining step for the photocatalytic reaction, we irradiated the samples after a 30 min stirring step in dark conditions. Degradation of AMX using the obtained photocatalysts showed the effect of a porous support type on the process efficiency. The synthesized photocatalysts were used in degradation of AMX under UV and visible light irradiation. The obtained results are shown in Figure 9A,B.

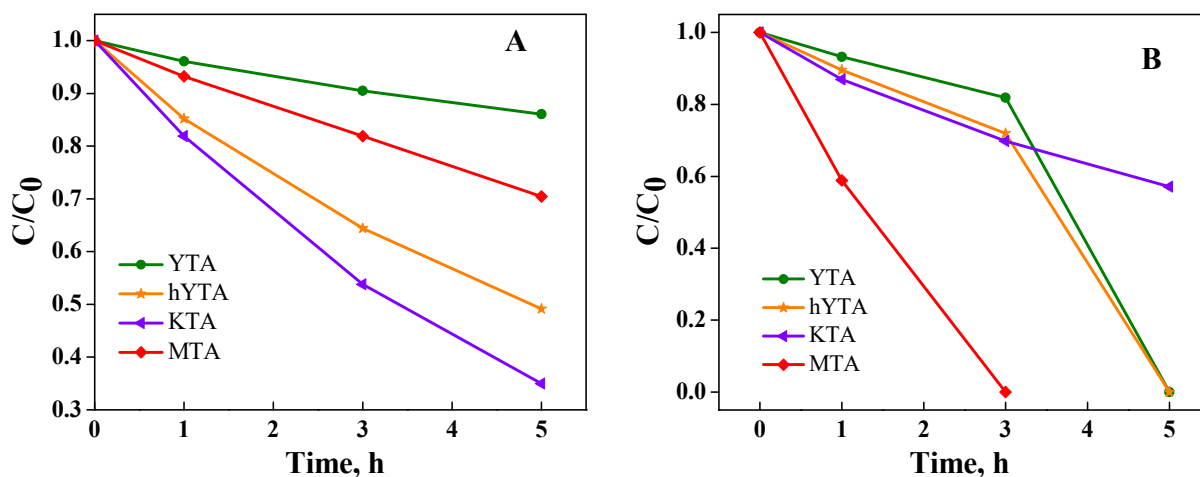


Figure 9. Photocatalytic degradation of amoxicillin under UV irradiation (A) and visible light (B) irradiation.

Under UV light irradiation, the best results in AMX degradation were obtained for the KTA sample (Figure 9A), with the highest titania dispersion (wide angle XRD—Figure 1A and Raman results—Figure 5) and highest percent of Au metallic nanoparticles on the surface (XPS results—Table 1). A better photoactivity obtained for the sample with smaller size of active species is in accordance with the other reported results [10]. This sample also presents larger ordered mesopores (Figure 1B, Table S1). The lowest photocatalytic degradation of AMX was obtained using the YTA sample, with small pore size. These results suggest an important effect of support textural properties, such as pore size, on obtaining active photocatalysts.

Under visible light irradiation, the best results were obtained for the MTA photocatalyst (Figure 9B). It is the only sample that contains anatase and rutile as titania crystalline species, according to the XRD and Raman results. Further, on the lower surface area of the MTA sample, the highest percent of metallic gold clusters (XPS results—Table 1) was evidenced. The rate of the photocatalytic reaction for this sample is significantly higher (3 h) and, unlike the others, less influenced by the adsorption process. Under these conditions, gold species absorbed the visible light and the photons induced an efficient separation of electron holes. The plasmon-induced electrons in Au NP clusters were transported to CB of TiO₂ and reacted with adsorbed oxygen, forming $\cdot\text{O}^{2-}$ active species.

After 5 h of visible light irradiation (Figure 9B), the lowest AMX degradation efficiency was obtained for KTA samples with the lowest titania content and highest percent of Au metallic nanoparticles on the surface. In this case, the activity is determined by the nature of the titanium species. In these samples, the majority are Ti-O-Si species, more active in photocatalytic reactions performed under UV light (KTA sample—Figure 9A).

The photocatalytic performances of the synthesized materials were also evaluated through the AMX degradation kinetics studies. The kinetics results obtained under UV and visible light irradiation are presented in Figure 10A,B. The AMX degradation in the presence of Ti-Au photocatalysts follows a pseudo first-order mechanism, expressed as $-\ln(C/C_0) = k_{\text{app}}t$. The high values of linear regression coefficients (R^2) of the kinetic plots confirm that photocatalytic degradation process of AMX using all the synthesized materials follows the pseudo first-order reaction, as reported by previous studies for photocatalytic

degradation of AMX [62]. The values of apparent rate constant (k_{app}) of the studied systems are presented in Figure 10A,B.

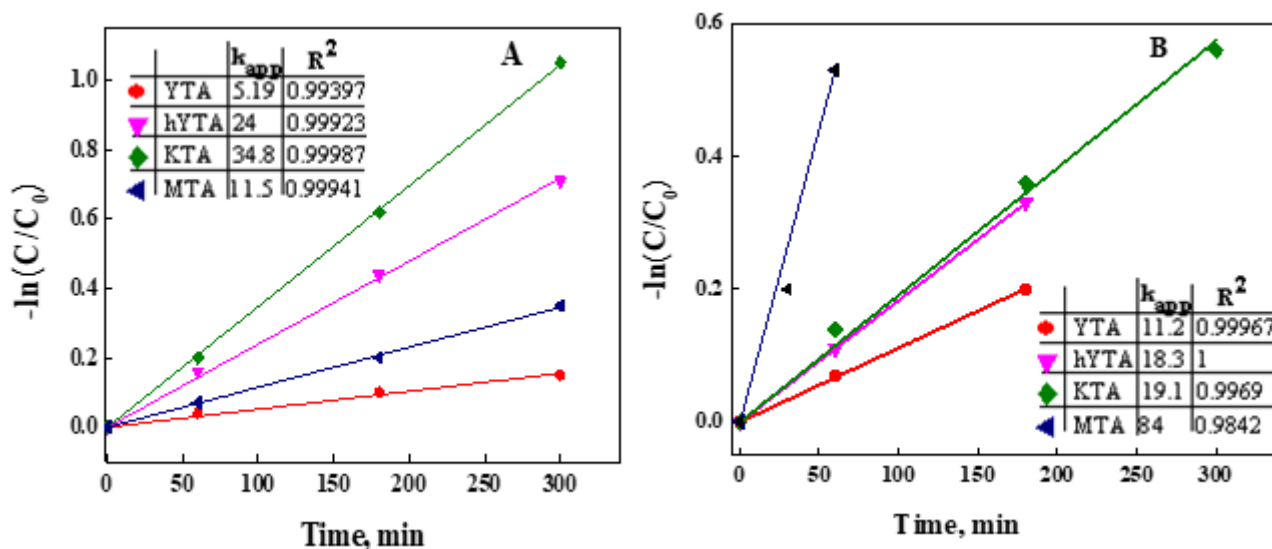


Figure 10. Kinetic and apparent rate constant k_{app} values ($\times 10^{-4} \text{ min}^{-1}$) of AMX photocatalytic degradation under UV (A) and visible light (B) irradiation.

Comparing the apparent rate constants obtained under UV light irradiation, it can be seen (Figure 10A) that KTA is 1.5-, 3- and 6-times higher more photoactive than hYTA, MTA and YTA, respectively. In the case of visible light irradiation, the photocatalytic process is promoted via plasmon activation of the Au NPs [63], followed by injection of photogenerated electrons in the conduction band of TiO_2 . In these conditions, the best photocatalytic activity was obtained for the MTA sample with the highest value of k_{app} ($88.3 \times 10^{-4} \text{ min}^{-1}$), due to the presence of TiO_2 as a mixture of anatase and rutile phase, as Raman spectra showed (Figure 5). This behavior indicates that the presence of a mixed anatase/rutile TiO_2 near Au NP is a crucial factor, leading to a synergistic electron transfer, which enhances the photocatalytic performance. There is a consecutive electron transfer from photoactivated Au NPs to rutile and then to adjacent anatase TiO_2 phase [63]. It was noticed that the mixed anatase/rutile TiO_2 phases have a high photocatalytic activity comparatively with anatase or rutile single phases [64]. The explanation proposed and widely accepted in the literature is based on a favorable contact between anatase and rutile phases, which ensures the electron transfer, leading to a better separation of photogenerated charge [64].

The kinetics results evidenced that hierarchical structure of zeolite Y leads to an increase in the apparent rate constant k_{app} , probably due to the improvement in accessibility degree of AMX molecules to the active sites.

Gold immobilization on supported TiO_2 nanoparticles extends the sensitivity of the photocatalysts into the visible domain and increases their photoactivity through electron injection from activated Au species into the conduction band of the semiconductor. The coupling of electromagnetic field of the incident visible light with oscillations in the electrons in Au NPs leads to an enhancement in electromagnetic fields near the Au NP surface [65]. In the case of UV irradiation, Au NPs act as an electron trap for photogenerated electrons from TiO_2 , avoiding electron-hole recombination. Generally, noble metals are used in photocatalyst synthesis to facilitate electron capture by forming a Schottky barrier on the metal–semiconductor junction [66]. Au produces the highest Schottky barrier among noble metals [65].

Although high values of amoxicillin degradation were obtained for catalysts as KTA, MTA and hYTA, total mineralization was not achieved. Therefore, the lowest value of total organic carbon elimination (TOC/TOC_0) was 0.6 for the hYTA sample after 5 h under UV

light irradiation. The low degree of mineralization was also indicated in other studies [55] and has been assigned to certain products more resistant to further oxidation. However, these products may be more biodegradable and bacteria or fungi can mineralize them [67]. The employed HPLC analytical method allowed for the detection of 6 products after AMX degradation under UV irradiation and 11 after its degradation under visible light. Most of them had smaller peak areas. We compared these results with those reported in the literature about amoxicillin degradation products [68–70], which indicate great diversity in intermediates resulting from AMX degradation. The proposed possible reaction pathway showed hydroxylation as the first step of degradation. The HO· radical plays a major role in the attack of benzoic ring or nitrogen moiety of AMX, which possess electrophilic characteristics [69]. Opening of the β -lactam ring of AMX by destruction of lactamic bond can be another pathway for AMX degradation. In the slightly basic conditions of the photocatalytic reactions (pH~8), the hydrolysis of AMX is activated. Furthermore, basic properties of the photocatalyst surface can favor the adsorption of C=O from β -lactam ring of AMX with more electrophilic properties. Nevertheless, the study of [55] showed that hydrolysis may contribute significantly to overall degradation of AMX under chosen irradiation conditions.

2.3. Proposed Mechanism for the Photocatalytic Degradation of AMX

It was previously reported by our group [16] that the photodegradation process of organic molecules as AMX was carried out through highly oxidative species as $\cdot\text{O}_2^-$ and HO· radicals, obtained due to the presence of photogenerated charge carriers. Other studies highlighted that AMX photodegradation is mainly due to the reactive species produced during irradiation (e.g., hydroxyl radical, hole and superoxide ion) [68]. Figure 11 shows a schematic representation of the proposed mechanism for photocatalytic degradation of AMX using materials synthesized in this study.

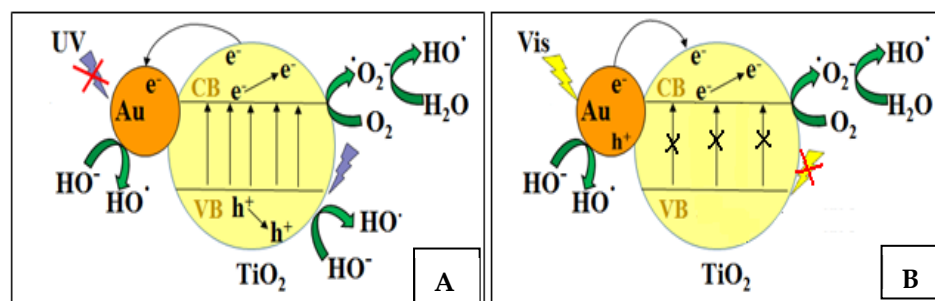


Figure 11. Schematic representation of the proposed mechanism for photocatalytic degradation of AMX under UV (A) and visible light irradiation (B).

Depending on light irradiation domain, the photocatalytic process could be explained by different roles of Au NPs, which act as electron traps in the case of UV irradiation or as an electron generator under visible light irradiation. When a photocatalytic experiment is carried out under UV irradiation (Figure 11A), TiO₂ nanoparticles are activated and there is an electron transfer from the valence band to the conduction band, leading to the formation of photogenerated charge carriers. Au NPs act as an electron trap, improving the separation of e⁻/h⁺ pairs. Therefore, unpaired electrons are used to obtain superoxide species ($\cdot\text{O}_2^-$) through reduction of O₂ molecules adsorbed on the photocatalyst surface, while unpaired holes ensure the oxidation process of hydroxyl ions from aqueous medium to HO· radicals, responsible for AMX degradation. On the other hand, in the case of visible irradiation (Figure 11B), the activated species are Au NPs through the SPR effect. The photogenerated hot electrons from gold nanoparticles are injected into the conduction band of TiO₂ and used to obtain highly reactive oxygen species as $\cdot\text{O}_2^-$ and HO· after reduction of adsorbed oxygen molecules. Further, h⁺ species remained in Au NPs after electron transfer is used to oxidize hydroxyl ions to HO· radicals.

Degradation efficiency is influenced among other important physico-chemical parameters of photocatalysts by the reactive oxygen species production under light irradiation, their number and the photocatalytic process time. Amoxicillin degradation occurs in several steps, the possible reaction products being AMX diketopiperazine, AMX penicilloic acid, phenol hydroxypyrazine, AMX S-oxide and AMX penilloic acid [69,70]. The variation in inhibition percentage with the irradiation conditions (UV and visible light) may be explained by different contributions of $\cdot\text{O}_2^-$ and $\text{HO}\cdot$ reactive species. The previous studies on the photocatalytic activity of supported titanium oxide [13] evidenced the main contribution of $\text{HO}\cdot$ reactive species to degradation of organic pollutants. In conditions of UV light and slightly alkaline pH, these radicals favor the hydrolysis reactions for the adsorbed amoxicillin molecules. In this way, AMX penicilloic acid, phenol hydroxypyrazine, AMX penilloic acid and AMX diketopiperazine can be obtained. These products, without β -lactamic ring, do not have an inhibitory effect against bacteria. Under visible light irradiation, the presence of gold, which induces the plasmonic effect, favors the formation of $\cdot\text{O}_2^-$ species that can lead to oxidation compounds containing the β -lactam ring as AMX S-oxide with an inhibitory effect.

3. Materials and Methods

3.1. Materials

The chemicals used in the photocatalyst synthesis are: sodium silicate solution ($\text{Na}_2\text{O}(\text{SiO}_2)_x \cdot x\text{H}_2\text{O}$, reagent grade), sodium aluminate (NaAlO_2), tetraethyl orthosilicate—TEOS ($\text{Si}(\text{OC}_2\text{H}_5)_4$, reagent grade, 98%), sodium hydroxide (NaOH , $\geq 98\%$), ethanol ($\text{CH}_3\text{CH}_2\text{OH}$, $>99.8\%$), 1-butanol ($\text{CH}_3(\text{CH}_2)_3\text{OH}$, anhydrous, 99.8%), tetradecyltrimethylammonium bromide—TTAB ($\text{CH}_3(\text{CH}_2)_{13}\text{N}(\text{Br})(\text{CH}_3)_3$, for synthesis), cetyltrimethylammonium bromide—CTAB ($\text{CH}_3(\text{CH}_2)_{15}\text{N}(\text{Br})(\text{CH}_3)_3$, $\geq 98\%$) and triblock copolymer P123 (PEG-PPG-PEG, average $M_n \sim 5800$); all were purchased from Sigma Aldrich (Burlington, MA, USA). Titanium (IV) n-butoxide ($\text{Ti}(\text{OCH}_2\text{CH}_2\text{CH}_2\text{CH}_3)_4$, reagent grade, 97%) from ACROS Organics (Geel, Belgium) and chloroauric acid ($\text{HAuCl}_4 \cdot 3\text{H}_2\text{O}$, $\geq 99.9\%$ trace metals basis) from Fluka (NC, USA). The amoxicillin ($\text{C}_{16}\text{H}_{19}\text{N}_3\text{O}_5\text{S}$, 95.0–102.0% anhydrous basis) for photocatalytic reactions was a Sigma Aldrich product.

3.2. Synthesis of Materials

All porous supports used in this study were synthesized as previously reported by our group [7,13,16]. All the supports were obtained by hydrothermal treatment. For synthesis of MCM-48 mesoporous silica, a cationic surfactant (CTAB), dispersed in a basic medium, was used as template while KIT-6 was obtained in acidic condition, using a non-ionic surfactant (P123). In both cases, alcohol was used with a double role: solvent and co-surfactant (ethanol—EtOH for MCM-48 and butanol—BuOH for KIT-6). Hierarchical zeolite Y was obtained by a seed assisted method, in the presence of a cationic surfactant (TTAB). Zeolite Y was obtained similarly, but in the absence of the surfactant. Cubic mesoporous silica MCM-48 and KIT-6 was suggestively noted M and K, while zeolite Y materials with microporous and hierarchical structure were denominated Y and hY, respectively.

Titanium and gold active sites were incorporated in the obtained supports by post-synthesis method (impregnation). The cubic silica and zeolite Y supports were impregnated with titanium species from alcoholic solution of titanium (IV) n-butoxide obtaining samples with 10% TiO_2 loading. After impregnation, materials were kept for 24 h at room temperature, dried at 80°C and calcinated in air at 600° . The obtained samples were named YT, hYT, MT and KT and were used as supports for gold immobilization. Au was immobilized by a double-impregnation method using HAuCl_4 solution. The amount of gold precursor was equivalent to 1 wt.% of Au in each sample. In the second step the chlorine was removed using a Na_2CO_3 solution [35]. The obtained samples were washed with sodium carbonate solution and deionized water, centrifuged, dried overnight at room temperature and then at 120°C for 6 h. This method was chosen due to the advantage of preparation of highly

active materials by using a simple method and a suitable precursor for gold as chloroauric acid [26,35]. The obtained materials were named YTA, hYTA, MTA and KTA.

3.3. Characterization of Materials

The crystalline and ordered mesoporous structures of materials were examined at wide and low angles using powder X-ray diffraction (Rigaku Ultima IV diffractometer-Rigaku Corp., Tokyo, Japan-with Cu K α , $\lambda = 0.15406$ nm). Crystallite size of supported TiO₂ was calculated using Scherrer's formula along (101) direction: $D = k \cdot \lambda / (\text{FWHM}) \cdot \cos(\theta)$, where λ is the wavelength of the Cu K α radiation (1.54056 Å), FWHM is full width at half maximum of the intensity vs. 2θ profile, θ is Bragg's diffraction angle and k is the shape factor (0.9). Elemental analysis of the obtained samples was determined using Rigaku ZSX Primus II spectrometer and the textural properties were characterized by Micromeritics ASAP 2020. Morphology, sample composition, ordered porous structure, zeolite crystals and dispersion of gold nanoparticles were evidenced by scanning electron microscopy (ZEISS EVO LS10 SEM, Germany) and transmission electron microscopy (TECNAI 10 G2-F30 and F20 G2 TWIN Cryo-TEM -FEI with EDX, OR, USA).

Surface analysis was performed by X-ray photoelectron spectroscopy (XPS—PHI Quantera equipment, ON, Canada). The X-ray source was monochromatized Al K α radiation (1486.6 eV) and overall energy resolution was estimated at 0.6 eV by the full width at half-maximum (FWHM) of the Au4f7/2 photoelectron line (84 eV).

The interaction with light of photocatalysts was examined using Raman, UV-Vis diffuse reflectance (JASCO V570 spectrophotometer, Tokyo, Japan) and photoluminescence spectroscopy. Micro-Raman spectra were recorded by means of a RM-1000 Renishaw Raman (Renishaw, New Mills, Wotton-Under-Edge, UK) and a LabRam HR800 spectrometer (HORIBA FRANCE SAS, Palaiseau, France) equipped with CCD detectors and gratings of 2400 gr/mm. Two lasers, Ar⁺-ion and He-Cd operating at 514.5 nm and 325 nm, respectively, were used as exciting radiations through the 50 \times and 40 \times NUV microscope objectives manufactured by Leica (Leica, Wetzlar, Germany) and Olympus (Olympus Corporation, Tokyo, Japan). Owing to two BraggGrate filters, visible Raman spectra were recorded from 5 cm⁻¹ in order to access pore and nanoparticle size information. The UV-Vis diffuse reflectance spectra were recorded on a JASCO V570 spectrophotometer. The fluorescence spectra were recorded with an FLSP 920 spectrofluorimeter (Edinburgh Instruments, Livingston, UK). The excitation source was an Xe lamp, excitation wavelength 550 nm and spectra were recorded between 570 and 800 nm. The excitation and emission slits were of 10 nm for all measurements.

3.4. Adsorption and Photocatalytic Experiments

The adsorption and photocatalytic degradation of amoxicillin reactions were carried out in a dark room thermostated at 30 °C. Next, 20 mg of the photocatalyst was added in quartz microreactors with 10 mL aqueous solution of amoxicillin—AMX (30 mg/L)—under stirring. Before reaction, mixture was first stirred in darkness for 30 min in order to ensure adsorption of the AMX on photocatalyst surface. Then, the reaction mixture was irradiated under UV light ($\lambda = 254$ nm), using 2 \times 60 W halogen lamps, and laser-visible light (532 nm). At given irradiated time intervals (1, 3 and 5 h, respectively), 3 mL of suspension was taken out and the catalyst was separated from the suspension using Millipore syringe filter of 0.45 μ m. The absorbance (A) of solution was measured by JASCO V570 UV-Vis spectrophotometer and degradation process evaluated by the variation in the maximum absorbance of AMX ($\lambda = 230$ nm). To evaluate AMX degradation, the solution phase concentration C (mg/L) at moment t and initial concentration C_0 (mg/L) at $t = 0$ were used.

Considering the AMX degradation as a first-order reaction, the apparent rate constant (k_{app}) was calculated using the relation: $-\ln(C/C_0) = k_{\text{app}}t$, where k_{app} is the apparent rate constant of the photodegradation process, C_0 and C represent AMX concentrations (mg/L) at the initial time and a given time t (min), respectively.

For AMX degradation monitoring RigolL300 HPLC equipped with an UV-Vis diode-array detector (λ : 210; 240 and 274 nm) and a Zorbax SB-C18 column (Agilent, Santa Clara, CA, USA) was employed. The mobile phase was a mixture of phosphate-buffer solution (20 mM)/acetonitrile, with a ratio of 80/20, flowing with 1 mL/min. The mineralization degree was monitored by total organic carbon (TOC) analysis. The TOC value was calculated by subtracting the value of the total inorganic carbon (TIC) from the value of the total carbon (TC). TC and TIC measurements were performed using an HiPer TOC Thermo Electron analyzer based on carbon dioxide infrared absorption. For TC, the UV-Persulfate oxidation method was employed, while TIC method involves the sample acidification and quantification of the released CO₂. Prior to analysis, all the samples collected during the runs were filtered through 0.20 μ m regenerate cellulose filters. All chromatographic, TOC analyses and antibacterial activity were performed in duplicate.

4. Conclusions

High-performance photocatalysts were obtained by immobilization of Ti and Au NPs on different supports with specific structural, textural and morphological properties. For dispersion of Ti species and, implicitly, of Au NPs on the support, interaction between them and interaction of each one with the support are considered the key factors that have a synergistic effect on photocatalytic performances of synthesized materials. The pore size, surface and adsorption properties influence the photocatalytic process, both by providing active species available for AMX degradation, as well as by ensuring the reagent mass transfer. The best results (100% degradation efficiency) were obtained under visible light for samples with Au metallic clusters on the surface (XPS results). Between these samples, the highest apparent rate constant was obtained for that obtained by dispersion of Ti and Au on MCM-48 support, the only one containing both anatase and rutile as titania species. A high adsorption capacity was also evidenced for this sample. The reaction mechanism, in which Au is e⁻ trap in UV and e⁻ generator in visible light, explained the synergistic action of support, as Au and TiO₂ species in photocatalytic reactions.

Although high values of amoxicillin degradation were obtained, total mineralization was not achieved. The low degree of mineralization was assigned to certain products more resistant to further oxidation. A different number of AMX by-products was obtained under UV and visible light irradiation. These results were explained by the difference between reaction mechanisms under UV and visible light.

Supplementary Materials: The following supporting information can be downloaded at: <https://www.mdpi.com/article/10.3390/catal12101129/s1>, Figure S1: EDX results for KTA (A), hYTA (B), YTA (C) and MTA (D) samples and the TEM image of the evaluated area (Cu and C are components of TEM grid support for the powder of sample); Figure S2: TEM images of samples MTA (A,B) and hYTA (C,D), Figure S3: (a–d) Au 4f (7/2, 5/2) high resolution, deconvoluted XPS spectra for the synthesized samples, Figure S4: Ti2p (a), Si2p (b) and Al2p (c) high resolution XPS spectra, Figure S5: The deconvoluted O1s spectra for YTA (a), hYTA (b), MTA (c) and KTA (d), Figure S6: Raman spectra of the cubic mesoporous supported (M/K)TA photocatalysts (a), zeolite supported (hY/Y)TA photocatalysts (b) and Y, (Y/K)TA photocatalysts (c). λ_L is the laser excitation line and A is anatase, Figure S7: Chemical structure of amoxicillin (AMX), Figure S8: The processes that take place in the removal of amoxicillin (AMX) from water (YTA photocatalyst); Table S1: Texture properties of samples and TiO₂ crystallite size of the samples after each impregnation step.

Author Contributions: Conceptualization, V.P.; methodology, V.P. and G.P.; validation, V.P. and E.M.A.; formal analysis, G.P., I.A. and M.C.; investigation, G.P., E.M.A., E.B., S.S. and C.B.; data curation, G.P., E.M.A., I.A., E.B., A.B., D.C.C. and B.T.; writing—original draft preparation, G.P., E.M.A. and S.S.; writing—review and editing, V.P.; visualization, V.P.; supervision, V.P. All authors have read and agreed to the published version of the manuscript.

Funding: This research received no external funding.

Data Availability Statement: The data presented in this study are available on request from the corresponding author.

Acknowledgments: The authors are thankful for the financial support from EU (ERDF) INFRANANOCHEM–No. 19/01.03.2009 project. The research infrastructure developed through this project and POS-CCE “AGRI-FLUX” project, no. 645/18.03.2014, SMIS-CSNR 48695 was partially used for sample characterization. Further, the authors would like to thank Alin Enache (Apel Laser) for the visible light laser (DPSS-532-100, $\lambda = 532$ nm) needed for the photocatalytic experiments.

Conflicts of Interest: The authors declare no conflict of interest.

References

1. Yoshiiri, K.; Wang, K.; Kowalska, E. TiO₂/Au/TiO₂ Plasmonic Photocatalysts: The Influence of Titania Matrix and Gold Properties. *Inventions* **2022**, *7*, 54. [\[CrossRef\]](#)
2. Do, T.C.M.V.; Nguyen, D.Q.; Nguyen, K.T.; Le, P.H. TiO₂ and Au-TiO₂ Nanomaterials for Rapid Photocatalytic Degradation of Antibiotic Residues in Aquaculture Wastewater. *Materials* **2019**, *12*, 2434. [\[CrossRef\]](#) [\[PubMed\]](#)
3. Yang, C.; Kalwei, M.; Schüth, F.; Chao, K. Gold nanoparticles in SBA-15 showing catalytic activity in CO oxidation. *Appl. Catal. A* **2003**, *254*, 289–296. [\[CrossRef\]](#)
4. Moragues, A.; Puértolas, B.; Mayoral, Á.; Arenal, R.; Hungría, A.B.; Murcia-Mascarós, S.; Taylor, S.H.; Solsona, B.; García, T.; Amorós, P. Understanding the role of Ti-rich domains in the stabilization of gold nanoparticles on mesoporous silica-based catalysts. *J. Catal.* **2018**, *360*, 187–200. [\[CrossRef\]](#)
5. Luna, M.; Gatica, J.M.; Vidal, H.; Mosquera, M.J. Au-TiO₂/SiO₂ photocatalysts with NO_x depolluting activity: Influence of gold particle size and loading. *Chem. Eng. J.* **2019**, *368*, 417–427. [\[CrossRef\]](#)
6. Qi, F.; Wang, C.; Cheng, N.; Liu, P.; Xiao, Y.; Li, F.; Sun, X.; Liu, W.; Guo, S.; Zhao, X.-Z. Improving the performance through SPR effect by employing Au@SiO₂ core-shell nanoparticles incorporated TiO₂ scaffold in efficient hole transport material free perovskite solar cells. *Electrochim. Acta* **2018**, *282*, 10–15. [\[CrossRef\]](#)
7. Filip, M.; Todorova, S.; Shopska, M.; Ciobanu, M.; Papa, F.; Somacescu, S.; Munteanu, C.; Parvulescu, V. Effects of Ti loading on activity and redox behavior of metals in PtCeTi/KIT-6 catalysts for CH₄ and CO oxidation. *Catal. Today* **2018**, *306*, 138–144. [\[CrossRef\]](#)
8. Rizzi, F.; Castaldo, R.; Latronico, T.; Lasala, P.; Gentile, G.; Lavorgna, M.; Striccoli, M.; Agostiano, A.; Comparelli, R.; Depalo, N.; et al. High Surface Area Mesoporous Silica Nanoparticles with Tunable Size in the Sub-Micrometer Regime: Insights on the Size and Porosity Control Mechanisms. *Molecules* **2021**, *26*, 4247. [\[CrossRef\]](#)
9. Lee, Y.Y.; Jung, H.S.; Kim, J.M.; Kang, Y.T. Photocatalytic CO₂ conversion on highly ordered mesoporous materials: Comparisons of metal oxides and compound semiconductors. *Appl. Catal. B Environ.* **2018**, *224*, 594–601. [\[CrossRef\]](#)
10. Sun, Z.; Bai, C.; Zheng, S.; Yang, X.; Frost, R.L. A comparative study of different porous amorphous silica mineral supported TiO₂ catalysts. *Appl. Catal. A Gen.* **2013**, *458*, 103–110. [\[CrossRef\]](#)
11. Vodyankin, A.A.; Vodyankin, O.V. The Effect of Support on the Surface Properties and Photocatalytic Activity of Supported TiO₂ Catalysts. *Key Eng. Mater.* **2016**, *670*, 224–231. [\[CrossRef\]](#)
12. Yadav, R.; Amoli, V.; Singh, J.; Tripathi, M.K.; Bhanja, P.; Bhaumik, A.; Sinha, A.K. Plasmonic gold deposited on mesoporous Ti_xSi_{1-x}O₂ with isolated silica in lattice: An excellent photocatalyst for photocatalytic conversion of CO₂ into methanol under visible light irradiation. *J. CO₂ Util.* **2018**, *27*, 11–21. [\[CrossRef\]](#)
13. Mureseanu, M.; Filip, M.; Somacescu, S.; Baran, A.; Carja, G.; Parvulescu, V. Ce, Ti modified MCM-48 mesoporous photocatalysts: Effect of the synthesis route on support and metal ion properties. *Appl. Surf. Sci.* **2018**, *444*, 235–342. [\[CrossRef\]](#)
14. Peng, R.; Zhao, D.; Dimitrijevic, N.M.; Rajh, T.; Koodali, R.T. Room Temperature Synthesis of Ti-MCM-48 and Ti-MCM-41 Mesoporous Materials and Their Performance on Photocatalytic Splitting of Water. *J. Phys. Chem. C* **2012**, *116*, 1605–1613. [\[CrossRef\]](#)
15. Jianga, C.; Lee, K.Y.; Parlett, C.M.A.; Bayazit, M.K.; Lau, C.C.; Ruan, Q.; Moniz, S.J.A.; Lee, A.F.; Tang, J. Size-controlled TiO₂ nanoparticles on porous hosts for enhanced photocatalytic hydrogen production. *Appl. Catal. A Gen.* **2016**, *521*, 133–139. [\[CrossRef\]](#)
16. Petcu, G.; Anghel, E.M.; Somacescu, S.; Preda, S.; Culita, D.; Mocanu, S.; Ciobanu, M.; Parvulescu, V. Hierarchical Zeolite Y Containing Ti and Fe Oxides as Photocatalysts for Degradation of Amoxicillin. *J. Nanosci. Nanotechnol.* **2020**, *20*, 1158–1169. [\[CrossRef\]](#) [\[PubMed\]](#)
17. Kim, M.-R.; Kim, S. Enhanced Catalytic Oxidation of Toluene over Hierarchical Pt/Y Zeolite. *Catalysts* **2022**, *12*, 622. [\[CrossRef\]](#)
18. Ayati, A.; Ahmadpour, A.; Bamoharram, F.F.; Tanhaei, B.; Manttari, M.; Sillanpaa, M. A review on catalytic applications of Au/TiO₂ nanoparticles in the removal of water pollutant. *Chemosphere* **2014**, *107*, 163–174. [\[CrossRef\]](#)
19. Zhu, H.; Chen, X.; Zheng, Z.; Ke, X.; Jaatinen, E.; Zhao, J.; Guo, C.; Xied, T.; Wangd, D. Mechanism of supported gold nanoparticles as photocatalysts under ultraviolet and visible light irradiation. *Chem. Commun.* **2009**, 7524, 7524–7526. [\[CrossRef\]](#)
20. Tang, K.Y.; Chen, J.X.; Legaspi, E.D.R.; Owh, C.; Lin, M.; Tee, I.S.Y.; Kai, D.; Loh, X.J.; Li, Z.; Regulacio, M.D.; et al. Gold-decorated TiO₂ nanofibrous hybrid for improved solar-driven photocatalytic pollutant degradation. *Chemosphere* **2021**, *265*, 129114. [\[CrossRef\]](#)
21. Sacaliuc, E.; Beale, A.M.; Weckhuysen, B.M.; Nijhuis, T.A. Propene epoxidation over Au/Ti-SBA-15 catalysts. *J. Catal.* **2007**, *248*, 235–248. [\[CrossRef\]](#)

22. Gutiérrez, L.F.; Hamoudi, S.; Belkacemi, K. Synthesis of Gold Catalysts Supported on Mesoporous Silica Materials: Recent Developments. *Catalysts* **2011**, *1*, 97–154. [[CrossRef](#)]
23. Zhou, J.; Yang, X.; Wang, Y.; Chen, W. An efficient oxidation of cyclohexane over Au@TiO₂/MCM-41 catalyst prepared by photocatalytic reduction method using molecular oxygen as oxidant. *Catal. Commun.* **2014**, *46*, 228–233. [[CrossRef](#)]
24. Xu, J.; Zhang, Z.; Wang, G.; Duan, X.; Qian, G.; Zhou, X. Zeolite crystal size effects of Au/uncalcined TS-1 bifunctional catalysts on direct propylene epoxidation with H₂ and O₂. *Chem. Eng. Sci.* **2020**, *227*, 115907. [[CrossRef](#)]
25. Liu, Z.; Shi, C.; Wu, D.; He, S.; Ren, B. A Simple Method of Preparation of High Silica Zeolite Y and Its Performance in the Catalytic Cracking of Cumene. *J. Nanotechnol.* **2016**, *2016*, 1486107. [[CrossRef](#)]
26. Basha, S.; Barr, C.; Keane, D.; Nolan, K.; Morrissey, A.; Oelgemoller, M.; Tobin, J.M. On the adsorption/photodegradation of amoxicillin in aqueous solutions by an integrated photocatalytic adsorbent (IPCA): Experimental studies and kinetics analysis. *Photochem. Photobiol. Sci.* **2011**, *10*, 1014–1022. [[CrossRef](#)]
27. Kozlova, A.; Kirik, S.D. Post-synthetic activation of silanol covering in the mesostructured silicate, materials MCM-41 and SBA-15. *Microporous Mesoporous Mater.* **2010**, *133*, 124–133. [[CrossRef](#)]
28. Kumar, D.; Schumacher, K.; du Fresne von Hohenesche, C.; Grun, M.; Unger, K.K. MCM-41, MCM-48 and related mesoporous adsorbents: Their synthesis and characterization. *Colloids Surf. A Physicochem. Eng. Asp.* **2001**, *187–188*, 109–116. [[CrossRef](#)]
29. Kishor, R.; Singh, S.B.; Ghoshal, A.K. Role of metal type on mesoporous KIT-6 for hydrogen storage. *Int. J. Hydrogen Energy* **2018**, *43*, 10376–10385. [[CrossRef](#)]
30. Duan, Y.; Zhai, D.; Zhang, X.; Zheng, J.; Li, C. Synthesis of CuO/Ti-MCM-48 Photocatalyst for the Degradation of Organic Pollutions Under Solar-Simulated Irradiation. *Catal. Lett.* **2017**, *148*, 51–61. [[CrossRef](#)]
31. Purushothaman, R.; Palanichamy, M.; Bilal, I.M. Functionalized KIT-6/Terpolyimide Composites with Ultra-Low Dielectric Constant. *J. Appl. Polym. Sci.* **2014**, *131*, 40508. [[CrossRef](#)]
32. Naumkin, A.V.; Kraut-Vass, A.; Gaarenstroom, S.W.; Poell, C.J. *NIST X-ray Photoelectron Spectroscopy Database; Version 4.1; NIST Standard Reference Database NIST SRD 20*, National Institute of Standards and Technology: Gaithersburg, MD, USA, 2012.
33. Moulder, F.; Stickle, W.F.; Sobol, P.E.; Bomben, K.D. *Handbook of X-Ray Photoelectron Spectroscopy*, ULVAC-PHI, Inc, 370 Enzo, Chigasaki 253-8522, Japan; Perkin-Elmer Corporation: Eden Prairie, MN, USA, 1995.
34. Zhang, Y.; Liu, J.X.; Qian, K.; Jia, A.; Li, D.; Shi, L.; Hu, J.; Zhu, J.; Huang, X. Structure Sensitivity of Au-TiO₂ Strong Metal-Support Interactions. *Angew. Chem.* **2021**, *60*, 12074–12081. [[CrossRef](#)] [[PubMed](#)]
35. Perera, A.S.; Trogadas, P.; Nigra, M.M.; Yu, H.; Coppens, M.O. Optimization of mesoporous titanosilicate catalysts for cyclohexene epoxidation via statistically guided synthesis. *J. Mater. Sci.* **2018**, *53*, 7279–7293. [[CrossRef](#)] [[PubMed](#)]
36. Zhang, H.; Tang, C.; Lv, Y.; Gao, F.; Dong, L. Direct synthesis of Ti-SBA-15 in the self-generated acidic environment and its photodegradation of Rhodamine. *J. Porous Mater.* **2014**, *21*, 63–70. [[CrossRef](#)]
37. Montagna, M. Characterization of Sol-Gel Materials by Raman and Brillouin Spectroscopies. In *Handbook of Sol-Gel Science and Technology*; Klein, L., Aparicio, M., Jitianu, A., Eds.; Springer International Publishing: Cham, Switzerland, 2016; pp. 1–32.
38. Sauvajol, J.; Pelous, J.; Woignier, T.; Vacher, R. Low frequency Raman study of the harmonic vibrational modes in silica aerogels. *J. Phys. Colloq.* **1989**, *50*, 167–169. [[CrossRef](#)]
39. Machon, D.; Bois, L.; Fandio, D.J.J.; Martinet, Q.; Forestier, A.; LeFloch, S.; Margueritat, J.; Pischedda, V.; Morris, D.; Saviot, L. Revisiting Pressure-induced Transitions in Mesoporous Anatase TiO₂. *J. Phys. Chem. C* **2019**, *123*, 23488–23496. [[CrossRef](#)]
40. Ivanda, M.; Musić, S.; Gotić, M.; Turković, A.; Tonejc, A.M.; Gamulin, O. XRD, Raman and FT-IR spectroscopic observations of nanosized TiO₂ synthesized by the sol-gel method based on an esterification reaction. *J. Mol. Struct.* **1999**, *480*, 645–649. [[CrossRef](#)]
41. Zhu, K.-R.; Zhang, M.S.; Chen, Q.; Yin, Z. Size and phonon-confinement effects on low-frequency Raman mode of anatase TiO₂ nanocrystal. *Phys. Lett. A* **2005**, *340*, 220–227. [[CrossRef](#)]
42. Yang, X.; Wang, Y.; Zhang, L.; Fu, H.; He, P.; Han, D.; Lawson, T.; An, X. The Use of Tunable Optical Absorption Plasmonic Au and Ag Decorated TiO₂ Structures as Efficient Visible Light Photocatalysts. *Catalysts* **2020**, *10*, 139. [[CrossRef](#)]
43. Georgescu, D.; Baia, L.; Ersen, O.; Baia, M.; Simon, S. Experimental assessment of the phonon confinement in TiO₂ anatase nanocrystallites by Raman spectroscopy. *J. Raman Spectrosc.* **2012**, *43*, 876–883. [[CrossRef](#)]
44. Wang, T.; Luo, S.; Tompsett, G.A.; Timko, M.T.; Fan, W.; Auerbach, S.M. Critical Role of Tricyclic Bridges Including Neighboring Rings for Understanding Raman Spectra of Zeolites. *J. Am. Chem. Soc.* **2019**, *141*, 20318–20324. [[CrossRef](#)] [[PubMed](#)]
45. Luan, Z.; Maes, E.M.; van der Heide, P.A.W.; Zhao, D.; Czernuszewicz, R.S.; Kevan, L. Incorporation of Titanium into Mesoporous Silica Molecular Sieve SBA-15. *Chem. Mater.* **1999**, *11*, 3680–3686. [[CrossRef](#)]
46. Aguiar, H.; Serra, J.; González, P.; León, B. Structural study of sol-gel silicate glasses by IR and Raman spectroscopies. *J. Non-Cryst. Solids* **2009**, *355*, 475–480. [[CrossRef](#)]
47. Liu, Q.; Li, J.; Zhao, Z.; Gao, M.; Kong, L.; Liu, J.; Wei, Y. Design, synthesis and catalytic performance of vanadium-incorporated mesoporous silica KIT-6 catalysts for the oxidative dehydrogenation of propane to propylene. *Catal. Sci. Technol.* **2016**, *6*, 5927–5941. [[CrossRef](#)]
48. Fan, F.; Feng, Z.; Li, C. UV Raman Spectroscopic Studies on Active Sites and Synthesis Mechanisms of Transition Metal-Containing Microporous and Mesoporous Materials. *Acc. Chem. Res.* **2010**, *43*, 378–387. [[CrossRef](#)]
49. Ricchiardi, G.; Damin, A.; Bordiga, S.; Lamberti, C.; Spano, G.; Rivetti, F.; Zecchina, A. Vibrational Structure of Titanium Silicate Catalysts. A Spectroscopic and Theoretical Study. *J. Am. Chem. Soc.* **2001**, *123*, 11409–11419. [[CrossRef](#)]

50. Parvulescu, V.; Ciobanu, M.; Petcu, G. Immobilization of semiconductor photocatalysts. In *Handbook of Smart Photocatalytic Materials Fundamentals, Fabrications, and Water Resources Applications*; Hussain, C.M., Mishra, A.K., Eds.; Elsevier: Amsterdam, The Netherlands, 2020.
51. Zhu, Q.; Lu, J.; Wang, Y.; Qin, F.; Shi, Z.; Xu, C. Burstein-Moss Effect Behind Au Surface Plasmon Enhanced Intrinsic Emission of ZnO Microdisks. *Sci. Rep.* **2016**, *6*, 36194. [[CrossRef](#)]
52. Wojcieszak, D.; Kaczmarek, D.; Domaradzki, J.; Mazur, M. Correlation of Photocatalysis and Photoluminescence Effect in Relation to the Surface Properties of TiO₂:Tb Thin Films. *Int. J. Photoenergy* **2013**, *2013*, 526140. [[CrossRef](#)]
53. Liqiang, J.; Yichun, Q.; Baiqi, W.; Shudan, L.; Baojiang, J.; Libin, Y.; Wei, F.; Honggang, F.; Jiazhong, S. Review of photoluminescence performance of nano-sized semiconductor materials and its relationships with photocatalytic activity. *Sol. Energy Mater. Sol. Cells* **2006**, *90*, 1773–1787. [[CrossRef](#)]
54. De Lourdes Ruiz Peralta, M.; Pal, U.; Sanchez Zeferino, R. Photoluminescence (PL) Quenching and Enhanced Photocatalytic Activity of Au-Decorated ZnO Nanorods Fabricated through Microwave-Assisted Chemical Synthesis. *ACS Appl. Mater. Interfaces* **2012**, *4*, 4807–4816. [[CrossRef](#)]
55. Kanakaraju, D.; Kockler, J.; Motti, C.A.; Glass, B.D.; Oelgemoller, M. Titanium dioxide/zeolite integrated photocatalytic adsorbents for the degradation of amoxicillin. *Appl. Catal. B Environ.* **2014**, *166–167*, 45–55. [[CrossRef](#)]
56. Nairi, V.; Medda, L.; Monduzzi, M.; Salis, A. Adsorption and release of ampicillin antibiotic from ordered mesoporous silica. *J. Colloid Interface Sci.* **2017**, *497*, 217–225. [[CrossRef](#)] [[PubMed](#)]
57. de Sousa, D.N.R.; Insa, S.; Mozeto, A.A.; Petrovic, M.; Chaves, T.F.; Fadini, P.S. Equilibrium and kinetic studies of the adsorption of antibiotics from aqueous solutions onto powdered zeolites. *Chemosphere* **2018**, *205*, 137–146. [[CrossRef](#)] [[PubMed](#)]
58. Kuzniatsova, T.; Kim, Y.; Shqau, K.; Dutta, P.K.; Verweij, H. Zeta potential measurements of zeolite Y: Application in homogeneous deposition of particle coatings. *Micropor. Mesopor. Mat.* **2007**, *103*, 102–107. [[CrossRef](#)]
59. Chinh, V.D.; Broggi, A.; Di Palma, L.; Scarsella, M.; Speranza, G.; Vilardi, G.; Thang, P.N. XPS Spectra Analysis of Ti²⁺, Ti³⁺ Ions and Dye Photodegradation Evaluation of Titania-Silica Mixed Oxide Nanoparticles. *J. Electron. Mater.* **2018**, *47*, 2215–2224. [[CrossRef](#)]
60. Liu, W.; He, T.; Wang, Y.; Ning, G.; Xu, Z.; Chen, X.; Hu, X.; Wu, Y.; Zhao, Y. Synergistic adsorption-photocatalytic degradation effect and norfoxacin mechanism of ZnO/ZnS@BC under UV-light irradiation. *Sci. Rep.* **2020**, *10*, 11903. [[CrossRef](#)]
61. Emara, M.M.; Ali, S.H.; Hassan, A.A.; Kassem, T.S.E.; Van Patten, P.G. How does photocatalytic activity depend on adsorption, composition, and other key factors in mixed metal oxide nanocomposites. *Colloid Interface. Sci.* **2021**, *40*, 100341. [[CrossRef](#)]
62. Li, D.; Zhu, Q.; Han, C.; Yang, Y.; Jiang, W.; Zhang, Z. Photocatalytic degradation of recalcitrant organic pollutants in water using a novel cylindrical multi-column photoreactor packed with TiO₂-coated silica gel beads. *J. Hazard. Mater.* **2015**, *285*, 398–408. [[CrossRef](#)]
63. Tsukamoto, D.; Shiraishi, Y.; Sugano, Y.; Ichikawa, S.; Tanaka, S.; Hirai, T. Gold Nanoparticles Located at the Interface of Anatase/Rutile TiO₂ Particles as Active Plasmonic Photocatalysts for Aerobic Oxidation. *J. Am. Chem. Soc.* **2012**, *134*, 6309–6315. [[CrossRef](#)]
64. Siah, W.R.; Lintang, H.O.; Shamsuddin, M.; Yuliati, L. High photocatalytic activity of mixed anatase-rutile phases on commercial TiO₂ nanoparticles. *IOP Conf. Ser. Mater. Sci. Eng.* **2016**, *107*, 012005. [[CrossRef](#)]
65. Tseng, Y.H.; Chang, I.G.; Tai, Y.; Wu, K.W. Effect of surface plasmon resonance on the photocatalytic activity of Au/TiO₂ under UV/visible illumination. *J. Nanosci. Nanotechnol.* **2012**, *12*, 416–422. [[CrossRef](#)] [[PubMed](#)]
66. Chen, J.; Zhang, J.; Ye, M.; Rao, Z.; Tian, T.; Shu, L.; Lin, P.; Zeng, X.; Ke, S. Flexible TiO₂/Au thin films with greatly enhanced photocurrents for photoelectrochemical water splitting. *J. Alloys Compd.* **2020**, *815*, 152471. [[CrossRef](#)]
67. Wang, Y.; Chen, C.; Zhou, D.; Xiong, H.; Zhou, Y.; Dong, S.; Rittmann, B.E. Eliminating partial-transformation products and mitigating residual toxicity of amoxicillin through intimately coupled photocatalysis and biodegradation. *Chemosphere* **2019**, *237*, 124491. [[CrossRef](#)] [[PubMed](#)]
68. Elmolla, E.S.; Chaudhuri, M. Photocatalytic degradation of amoxicillin, ampicillin and cloxacillin antibiotics in aqueous solution using UV/TiO₂ and UV/H₂O₂/TiO₂ photocatalysis. *Desalination* **2010**, *252*, 46–52. [[CrossRef](#)]
69. Gozlan, I.; Rotstein, A.; Avisar, D. Amoxicillin-degradation products formed under controlled environmental conditions: Identification and determination in the aquatic environment. *Chemosphere* **2013**, *91*, 985–992. [[CrossRef](#)]
70. Mirzaei, A.; Chen, Z.; Haghghat, F.; Yerushalmi, L. Magnetic fluorinated mesoporous g-C₃N₄ for photocatalytic degradation of amoxicillin: Transformation mechanism and toxicity assessment. *Appl. Catal. B Environ.* **2019**, *242*, 337–348. [[CrossRef](#)]